Synchrotron x-ray topographic and high-resolution diffraction analysis of mask-induced strain in epitaxial laterally overgrown GaAs layers

R. Rantamäki[a] and T. Tuomi
Optoelectronics Laboratory, Helsinki University of Technology, P.O. Box 3000, FIN-02015 HUT, Finland

Z. R. Zytkiewicz and J. Domagala
Institute of Physics, Polish Academy of Sciences, Al. Lotnikow 32/46, 02-668 Warszawa, Poland

P. J. McNally
Microelectronics Research Laboratory, School of Electronic Engineering, Dublin City University, Dublin 9, Ireland

A. N. Danilewsky
D-79108 Freiburg, Germany

(Received 11 May 1999; accepted for publication 16 July 1999)

Synchrotron x-ray back reflection section topographs of epitaxial lateral overgrown (ELO) GaAs samples grown on (001) GaAs substrates show images of the GaAs layers bent due to the interaction between the layer and the SiO_2 mask. The topographs are simulated under the assumption of orientational contrast. Using the same data the measured x-ray diffraction curve is simulated. The calculations, which are in good agreement with the measurements, are used to gain information on the tilted (001) lattice planes in each ELO layer. We show that the bending of ELO lattice planes reaches a maximum at the center of the ELO stripes, where misorientation is at a minimum, and decreases towards the edges of the stripes, where misorientation reaches a maximum. © *1999 American Institute of Physics.* [S0021-8979(99)07320-X]

I. INTRODUCTION

A key advantage of the epitaxial lateral overgrowth (ELO) technique is a high efficiency of substrate defect filtration during the ELO growth.[1] During the ELO process layers are grown on a substrate covered by a mask in which seed windows are opened. The epitaxial layers start to grow vertically from the mask-free seed windows. Next, the growth proceeds laterally over the mask as vertical growth continues. If the growth time is long enough single ELO layers coalesce and full coverage of the substrate by the ELO layers is obtained. Some early investigations were carried out on Si[2] and on GaAs.[1,3,4] Lately, this technique has been applied to GaN and blue lasers have been produced on these ELO materials.[5] However, an understanding of the processes active during the ELO procedure is still far from complete. The question of the possible interaction of the ELO layer with the mask still seems to be open. This problem can be of prime importance if the final goal is to produce lasers or other devices on ELO wafers.

Using synchrotron x-ray topography[6] and high resolution x-ray diffraction (XRD) techniques we have shown recently[7,8] that the lattice planes of GaAs ELO layers grown on GaAs substrates are bent towards the mask in the plane perpendicular to the seed windows. This bending is due to the interaction between the closely spaced surfaces of laterally overgrown parts of the ELO layer and the SiO_2 mask. The bending strain disappears when the mask is removed by selective etching. The aim of this work is to show that using mathematical procedures the topographic images and diffraction curves can be simulated. In this way information is gained about the shape of deformed lattice planes of the ELO layers. Some conclusions are then made about the mechanism by which the bending of the ELO stripes occurs.

II. EXPERIMENT

The Si-doped GaAs ELO layers were grown by liquid phase epitaxy upon liquid encapsulated Czochralski (001) GaAs substrate possessing an etch pit density of $5\times10^4\,cm^{-2}$. Prior to epitaxy the substrate, having a thickness of 400 μm, was covered with a 0.1-μm-thick SiO_2 film and subsequently patterned by photolithography to open 10 μm wide parallel seed windows in the SiO_2 mask. The spacing between the adjacent seed windows was 500 μm and they were oriented 15° off the ⟨110⟩ direction. Details of the growth procedure can be found elsewhere.[9]

Synchrotron back reflection and back reflection section topography as well as XRD techniques were applied to the GaAs ELO sample. The topographs were produced with synchrotron radiation from the DORIS III storage ring bending magnet source at the HASYLAB–DESY (Hamburger Synchrotronstrahlungslabor am Deutschen Elektronen-Synchrotron) topography station F1. Positron currents of 70–140 mA were used and the particle momentum was 4.443 GeV/c. For back reflection topography, the beam size was limited to 3.6 mm×1.4 mm. In the back reflection section geometry, the beam was limited by a horizontal slit of length 3.6 mm and height 20 μm. The distance between the sample and the film, both perpendicular to the beam, was 41 mm. In both geometries the beam went through a hole cut in the

[a]Electronic mail: reko.rantamaki@hut.fi

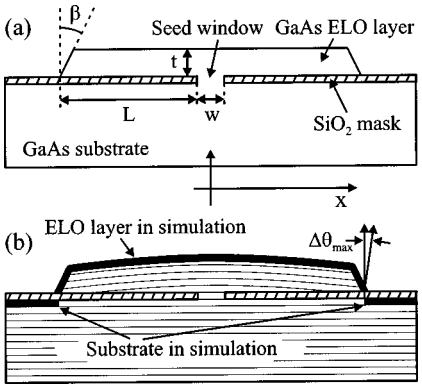

FIG. 1. Schematic cross section of the GaAs ELO sample, (a) structure of the sample and parameters: thickness *t*, seed window width *w*, width of the overgrown region *L*, and the slope angle β and (b) structure used for simulation (thick black lines). $\Delta\theta_{max}$ is the largest angle of rotation of the (001) lattice planes about an axis parallel to the seed windows.

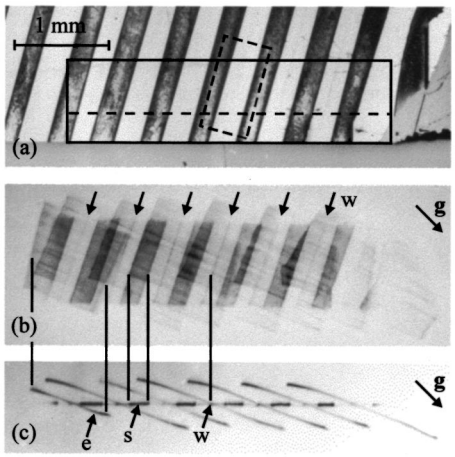

FIG. 2. GaAs ELO sample, (a) plane optical image (left and right inverted), the dashed line box shows the position of the XRD curve measurement, (b) 206 back reflection topograph [position marked as a solid line box in (a)] and (c) 206 back reflection section topograph [position marked as a dashed line in (a)]. The scale in (b) and (c) is the same as in (a), **g** is diffraction vector, *w* is seed window, *e* is ELO, and *s* is substrate.

center of the film, hit the sample, and was diffracted by the sample lattice planes. The backwards diffracted beams were recorded on the film, on which they formed a back reflection Laue pattern of spots called topographs. The ELO structure was on the film side of the sample. The sample was oriented with the [001] and [110] directions pointing towards the source and downwards, respectively. The direction of the ELO stripes deviated 15° counter clockwise from the vertical direction when looking from the film side. The topographs were recorded on Kodak high resolution SO-343 films.

The same sample was subsequently studied with the use of a high resolution x-ray diffractometer in the double axis configuration. The diffraction curves of 004 Cu $K\alpha_1$ reflections [(220) Ge monochromator] were obtained for the sample orientation in which the diffraction plane was set parallel to the seed windows. The diffracted beam intensity was measured as a function of angle of rotation $\Delta\theta$ about an axis parallel to the seed windows. The measurement spot was $1\,\text{mm}\times 0.5\,\text{mm}$.

Figures 1(a) and 1(b) show schematically the ELO structure and the lattice planes in the substrate and in a single ELO layer. Figure 1(a) defines the parameters: thickness *t*, seed window width *w*, width of the overgrown region *L*, and the slope angle β of the ELO sample. Figure 1(b) shows schematically the corresponding ELO structure used in computer simulations. $\Delta\theta$ is the tilt angle, i.e., angle of rotation about an axis parallel to the seed windows, of the (001) lattice planes of the ELO layers with respect to those of the substrate. It has the maximum value $\Delta\theta_{max}$ at the edge of the ELO stripe. $\Delta\theta$ is a function of distance *x* measured perpendicularly from the center of the stripe.

Figures 2(a), 2(b), and 2(c) show an optical micrograph (left and right inverted), 206 back reflection topograph and 206 back reflection section topograph, respectively, of the ELO sample. The 206 reflection was chosen for a detailed analysis of this work, because the ELO layer images are most pronounced with it, especially in the 206 back reflection section topograph of Fig. 2(c). In the optical image of Fig. 2(a) the area of the back reflection topograph of Fig. 2(b) has been marked with a bold box. The dotted line in Fig. 2(a) shows the image line of the back reflection section topograph of Fig. 2(c). The dotted box defines the area of the sample studied by XRD. Bright and dark areas in Fig. 2(a) are the ELO layers and the substrate stripes, respectively. The 206 back reflection topograph of Fig. 2(b) resembles the optical micrograph of Fig. 2(a). The dark stripes of Fig. 2(b) are the diffraction images of the substrate and an almost one-to-one correspondence exists between them and the optical images. The diffraction images of the ELO layers are seen as rather broad overlapping shadow-like images in the topograph because the Bragg reflected beam is diverged by the bent lattice planes. In the middle of each ELO stripe image the seed window can be observed as a narrow line marked with ''*w*'' arrows in Fig. 2(b). It is worth noticing that the blackening of the film slightly varies periodically along the ELO layer images. These variations can be explained by nonuniform bending of the ELO layer in the direction parallel to the seed windows. The 206 back reflection section topograph of Fig. 2(c) clearly shows the substrate as six short equally spaced horizontal lines marked as ''*s*'' and the ELO layers as six rather long curved lines marked as ''*e*.'' The images of the seed windows marked as *w* are seen as dots located between the substrate images. Vertical lines are drawn to facilitate the recognition of one broad ELO stripe image *e* in Fig. 2(b). Vertical lines are also drawn to identify one substrate *s* and one seed window *w* image.

From the section topograph presented in Fig. 2(c) we can obtain the largest value of misorientation for the ELO lattice planes. This is based on the observation that in our ELO sample the lattice tilt is greatest at the edges of the ELO stripe. These edges diffract the x-ray beam to the points at the ends of the ELO layer image. On the other hand we know that the image of the unbent ELO layer should be next to and parallel to the substrate images. Therefore, we can measure the distance between these two points on the film, which, in turn, can be converted into the value of maximum misorientation $\Delta\theta_{max}$ between the substrate and the ELO layer.

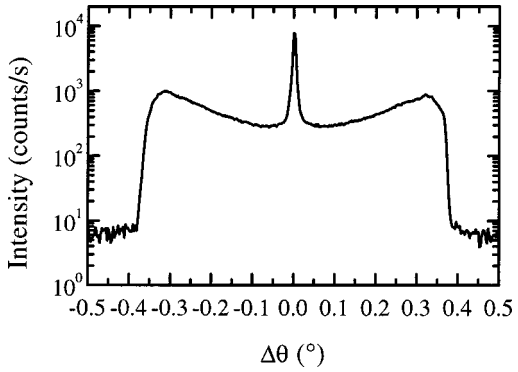

FIG. 3. Measured XRD intensity ($004\,\mathrm{Cu}\,K\alpha_1$) of a single GaAs ELO stripe as a function of angle of rotation $\Delta\theta$ of the (001) lattice planes about an axis parallel to the seed windows. The side lobes (maxima at $\Delta\theta = \pm 0.32°$) around the substrate peak (at $\Delta\theta = 0°$) are due to the ELO.

Figure 3 shows the 004 Cu $K\alpha_1$ diffraction curve taken from the piece of the sample marked by the dashed box in Fig. 2(a). It is clearly seen that the curve consists of a strong central peak due to the substrate and two side maxima due to the ELO at $\Delta\theta = \pm 0.32°$. Both the shape of the topographic image [Fig. 2(c)] as well as the structure of the diffraction curve apparently indicate the existence of crystal plane deformation in the ELO layer.

III. SIMULATION

The simulations presented in this work are based on the dimensions of the sample shown in Fig. 1(a): the ELO layer thickness t, the width of the seed window w, the width of the overgrown part of the layer L, and the ELO layer edge slope β. Other parameters used were the maximum misorientation $\Delta\theta_{\max}$ and the distance from the sample to the film. The tilt angle $\Delta\theta$ of the (001) planes is a function of distance x measured from the center of the ELO stripe in the direction perpendicular to the stripe. The $|\Delta\theta_{\max}|$ of the (001) ELO lattice planes with respect to the substrate at the edges $x = \pm(L + w/2)$ of the ELO layer is estimated from the back reflection section topographs. Figure 1(b) shows schematically the cross section of the ELO structure used for the simulations of the bending of the (001) lattice planes. Only the top surface of the ELO layer (curved black line), the edges of the ELO layer (straight black lines), and the substrate (straight black lines under the SiO_2 mask) are taken into account in the calculations. These three lines are simulated as a chain of 510 equally spaced points. Each of these points possesses a misorientation of (001) planes determined by its position x via the $\Delta\theta(x)$ function. Thus, the (001) planes at each simulation point i are rotated to a given misorientation $\Delta\theta_i$. The rotation axis is taken parallel to the seed windows. All other lattice plane normals are then calculated according to this rotation. Next, we calculate the angle θ_i between the [001] incident beam and the reflecting plane normal. The Bragg reflected beam at each point makes an angle of $2\theta_i$ with respect to the incident beam. Subsequently we calculated the positions of the 510 diffracted beams on the film, which form our simulated image.

TABLE I. Misorientation $\Delta\theta(x)$ of the (001) ELO lattice planes with respect to the (001) substrate planes across ELO stripes, $-(L + w/2) \leqslant x \leqslant (L + w/2)$, in Cases I–V. Axis of rotation is parallel to the seed windows.

Case	$\Delta\theta(x)$
I	$\Delta\theta_{\mathrm{I}}(x) = 0$
II	$\Delta\theta_{\mathrm{II}}(x) = kx$
III	$\Delta\theta_{\mathrm{III}}(\pm x) = \pm\Delta\theta_{\max}$, $\Delta\theta_{\mathrm{III}}(x = 0) = 0$
IV	$\Delta\theta_{\mathrm{IV}}(\pm x) = \pm\Delta\theta_{\max}\left[\sin\left(\frac{\pi}{2}\frac{\lvert x\rvert}{L + w/2}\right)\right]^{1/2}$
V	$\Delta\theta_{\mathrm{V}}(\pm x) = \pm\Delta\theta_{\max}\left\{1 - \left[\cos\left(\frac{\pi}{2}\frac{\lvert x\rvert}{L + w/2}\right)\right]^{1/2}\right\}$

The XRD curve is calculated using the same kinematical theory as in the simulation of topographs. The distribution of the misorientation values $\Delta\theta_i$ in all simulation points is plotted as a function of misorientation angle. This distribution can be interpreted as a diffraction curve simulation. X-ray absorption, lattice parameter changes due to doping, strain in the substrate, and strain effects other than the misorientation variation, $\Delta\theta(x)$, in the ELO stripe are omitted from the calculations.

IV. COMPARISON BETWEEN THEORY AND EXPERIMENT

In simulations we can create topographic images of ELO systems which do not necessarily exist in reality. However, analysis of these cases can help us to understand the behavior of real structures. At the outset, we will use a simple steplike edge model [$L = 143$, $t = 15$, $w = 10\,\mu\mathrm{m}$, $\Delta\theta_{\max} = 0.375°$, $\beta = 0°$ (no images from the edges)] instead of the sloped edge model, presented in Fig. 1(b), which will be used for more detailed simulations. There are three simple, but interesting cases which should be considered as a first approximation of real physical situations. The forms of the $\Delta\theta(x)$ functions are shown in Table I. In Case I there is no misorientation between the substrate and the ELO layer. In the ideal case, $\Delta\theta_{\mathrm{I}}(x) = 0$, the ELO lattice planes are not deformed at all and they are parallel to the substrate crystal planes. In Case II the misorientation is proportional to the distance x from the center of the seed window $\Delta\theta_{\mathrm{II}}(x) = kx$, where k is a constant. This corresponds to the ELO lattice planes which are uniformly bent in the direction perpendicular to the seed windows with curvature radius $R = 1/k$. Finally, we consider Case III in which the misorientation has only two values $-\Delta\theta_{\max}$ and $\Delta\theta_{\max}$ in the left and right half of the ELO stripe, respectively. Such a situation corresponds to the ELO structure with a triangle-like shape of the (001) crystal planes. Let us underline that Cases I and III set the limits within which the real $\Delta\theta(x)$ function should vary.

Figure 4(a) shows the misorientation as a function of the position across the ELO stripe in Cases I–III. Figure 4(b) shows simulated 206 topographs for those three situations. The thin lines in Figs. 4(a) and 4(b) show how Cases I and III set the limits to real $\Delta\theta(x)$ functions. In Case I the steplike image is due to the finite thickness of the ELO layer. In

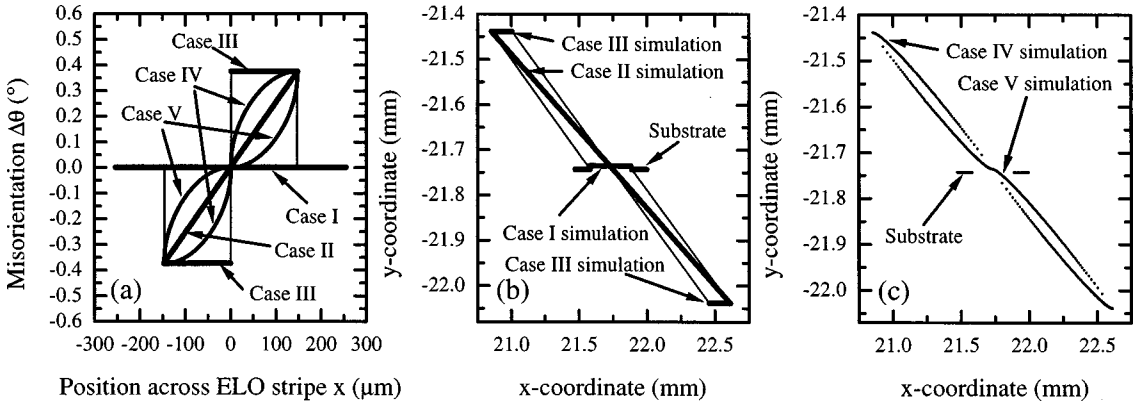

FIG. 4. Misorientation (a) in Cases I–V as a function of position, (b) simulation of 206 topograph in Cases I–III, and (c) simulation of 206 topographs in Cases IV and V. Thin lines in (a) and (b) show how Cases I and III set the limits to real $\Delta\theta(x)$ functions.

Case II the ELO layer image is seen as a long straight line. In Case III the calculated topograph of the ELO layer consists of two short lines far away from each other and from the image of the substrate.

The comparison of results shown in Fig. 4(b) with the back reflection section topograph of Fig. 2(c) apparently shows that from the $\Delta\theta(x)$ functions discussed up to now, the model of curved ELO crystal planes (Case II) fits best the real topographic image. However, a variation of the curvature radius R across the ELO stripe must be allowed if the nonlinear shape of the topographic image is to be simulated. Therefore, two additional $\Delta\theta(x)$ functions, namely for Cases IV and V (see Table I), were considered. As will be shown later, Case IV leads to the shape of simulated topograph, which agrees very well with the experimental one. The $\Delta\theta_V(x)$ function was chosen to represent the opposite, yet possible, physical behavior of the ELO stripes. The misorientations, $\Delta\theta_{IV}(x)$ and $\Delta\theta_V(x)$, for those two models are plotted in Fig. 4(a) as a function of the position across the ELO stripe. It is worth noting that $\Delta\theta_{IV}(x)$ increases rapidly near the seed window and slowly near the edge of the ELO layer. For $\Delta\theta_V(x)$ the situation is just the opposite—the misorientation increases slowly near the seed window and rapidly near the edge of the ELO layer. By analysis of the curvature radius functions ($R=ds/d\theta$, where ds is the separation and $d\theta$ is the change in the misorientation between adjacent simulation points) one can show that this corresponds to situations in which the (001) crystal planes' curvature radius is the smallest (bending is the largest) in the middle or at the edge of the ELO stripe for Cases IV and V, respectively.

Figure 4(c) shows the calculated 206 topographs for the Cases IV and V. Their intensity distributions and shapes are quite different. In the Case IV simulation there is more intensity at the ends than at the center of the ELO layer image. In the Case V simulation the intensity distribution is the opposite—there is more intensity in the middle rather than at the far ends of the ELO layer image. The shape of the Case IV simulation is smooth in the middle while the Case V simulation shows a distinctive kink at its center. It is quite clear that only the calculated Case IV image of Fig. 4(c) is similar to the measured back reflection section topograph of Fig. 2(c). The shape of the image and the intensity distribution of Case IV both fit well to the topograph observed. Moreover, the kink predicted by the Case V simulation is missing in the image of Fig. 2(c).

Figures 5(a) and 5(b) show the distribution of the $\Delta\theta_i$ values, which can be interpreted as a simulation of (004) rocking curves, calculated for Cases IV and V, respectively. In agreement with the topographic image simulations, we see that Case IV is the only one which qualitatively reproduces the main features found in the experimental curve of Fig. 3. The sharp peak in the middle is due to the substrate between the ELO layers. The side maxima and the proper intensity distribution are observed only when the ELO layer misorientation increases strongly near the center and weakly near the

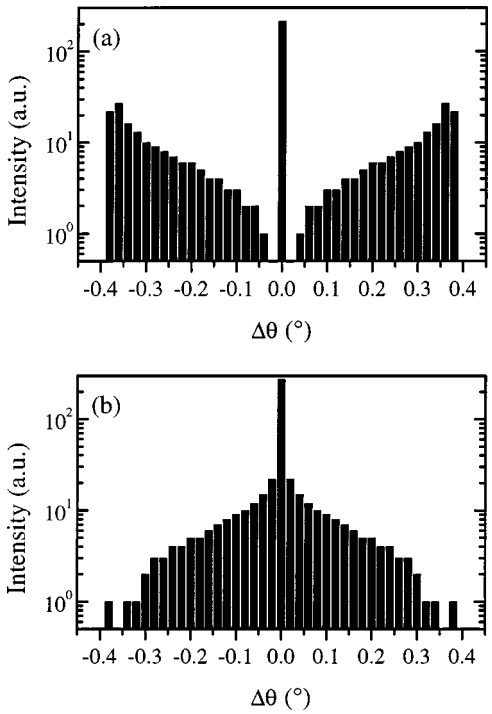

FIG. 5. Calculated XRD intensity of 004 XRD of the GaAs ELO sample as a function of angle of rotation $\Delta\theta$ of (001) lattice planes about an axis parallel to the seed windows, (a) in Case IV and (b) in Case V. The central peak is due to the substrate and the side lobes are due to the bent ELO layer.

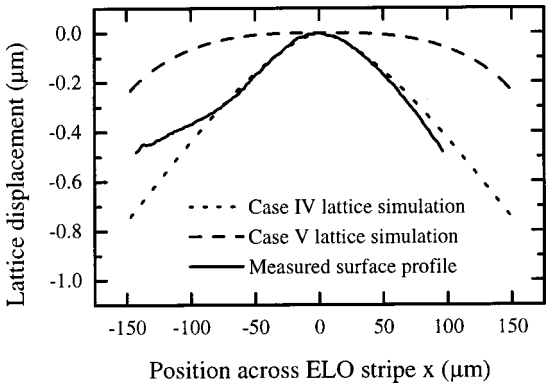

FIG. 6. Calculated lattice displacement of the ELO layers in Cases IV and V and the measured surface profile of a single GaAs ELO stripe as a function of distance x from center of ELO stripe.

edges. The angular separation of the side maxima is equal to $2\Delta\theta_{\max}$.

It is worth noting that once the $\Delta\theta(x)$ function is obtained the deformation of ELO lattice planes can be calculated. Only the spacing of simulation points and $\Delta\theta_i$ for each point have to be known when constructing the lattice plane image. Figure 6 shows the form of the (001) crystal planes of Cases IV and V and the shape of the ELO stripe surface in the direction perpendicular to the seed windows. The shape of the ELO surface was measured using a surface profilometer. The measurement was performed on the ELO stripe within the dashed box in Fig. 2(a). In order to remain within the high sensitivity range of the system, only the central part of that particular ELO stripe was measured. The plot of the surface scan was shifted to adjust its maximum to the maximum of the calculated curve. From Fig. 6 it is clear that the experimental profile near the seed window is quite similar to that predicted by the Case IV simulation. The largest bending was found in the middle part of the layer, which is opposite to the behavior calculated in the Case V model. It is important to point out here that the upper surface of the ELO layer does not necessarily represent the atomically flat (001) crystal plane precisely, as the dislocations propagating through the seed window from the substrate supply steps to the surface. Although this effect may be present Fig. 6 indicates that in our sample surface steps or steps bunches have a minor influence on the shape of the macroscopic surface profile.

Let us mention that a similar microscopic deformation has been observed recently by monochromatic x-ray beam topography for Si lamellae grown by the liquid phase ELO technique on thermally oxidized silicon substrates.[10,11] The effect of bending has been explained as being due to the surface tension forces of the melt, which bend the ELO stripes towards the mask. As soon as the surfaces of the ELO layer and the masking film are close enough the van der Waals attractive forces keep them together via the same mechanism as exploited in the wafer bonding technique. Although such an interpretation sounds reasonable its experimental verification is still missing. However, in the framework of this model, one should expect that bending of the ELO stripes would start at the beginning of growth when the

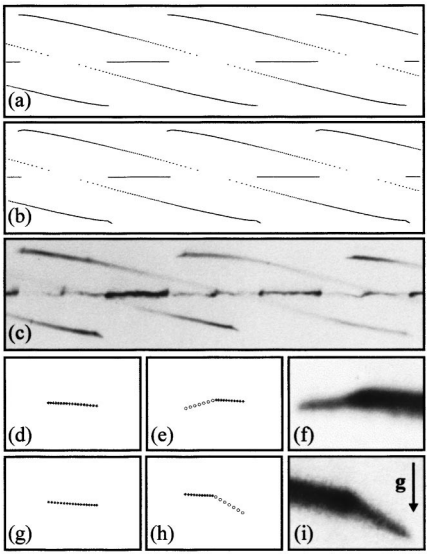

FIG. 7. Simulated 117 back reflection section topograph (a) in the case of step edge model, (b) in case of sloped edge model, and (c) measured 117 back reflection section topograph. Figures 7(d), 7(e), and 7(f) show enlargements of the upper ends and Figs. 7(g), 7(h), and 7(i) enlargements of the lower ends of the streaks shown in Figs. 7(a), 7(b), and 7(c), respectively. Width of the small and large images is about 60 μm and 1.4 mm, respectively. **g** is diffraction vector.

laterally overgrown parts of the layer are very thin and flexible. Then, the bent crystal planes might be reproduced during subsequent growth, though still retaining their shape. The shape of ELO lattice planes shown in Fig. 6 is in favor of such a postulation.

The question arises as to what extent the assumption of the step-like shape of the ELO stripe edge affects the results obtained. To analyze the contribution of the edge we calculated the ELO layer image similar to Fig. 2(c) using the structural parameters of a particular stripe: $L=143$, $t=15$, $w=10\,\mu$m, $\beta=27.5°$, $\Delta\theta_{\max}=0.375°$, $\Delta\theta=\pm0.37°$ in the upper corners at $x=\pm x_1=\pm(L+w/2-t\tan\beta)$ of the ELO stripe and the $\Delta\theta_{\mathrm{IV}}(x)$ function for $-x_1\leqslant x\leqslant x_1$ and the $\Delta\theta_{\mathrm{II}}(x)$ function for $-(L+w/2)\leqslant x<-x_1$ and for $x_1<x\leqslant(L+w/2)$. Figures 7(a) and 7(b) show the 117 topographic images calculated according to the step-like ($\beta=0°$) and inclined edge ($\beta=27.5°$) models, respectively. Figure 7(c) shows the 117 back reflection section topograph of the ELO stripe. The ends of the streaks are enlarged in Figs. 7(d)–7(i) for easier comparison. Figures 7(d), 7(e), and 7(f) show enlargements of the upper ends and Figs. 7(g), 7(h), and 7(i) enlargements of the lower ends of the streaks shown in Figs. 7(a), 7(b), and 7(c), respectively. It can be easily noticed that the overall shape of the simulated images of Figs. 7(a) and 7(b) is the same. The only difference is the appearance of the kinks close to the ends of the ELO streaks when the observed value of the edge slope is put into the simulation. It is important to underline that such kinks are in fact present in the image shown in Figs. 7(c), 7(f), and 7(i). In the framework of our approach, x-ray reflections from the edges of the ELO stripe are their origin. In the same way the edge effect may partly influence the shape of the diffraction curve shown in Fig. 3. The small broadening visible outside the side maxima

can partly be attributed to the thin edge of the ELO stripe. Although the misorientation has its maximum at the edge, the diffracting volume is small there. Therefore, the edge effect contribution is visible as a small broadening outside the side maxima, only.

It may seem that the XRD measurements and the results obtained from topographs disagree, because the separation of the central peak and the side maxima $\Delta\theta = 0.32°$ in the XRD measurements, while we obtain $\Delta\theta_{max} = 0.375°$ from the topographs. However, we should not compare these two values directly, because they represent different measurements. The total width of the diffraction curve in Fig. 3 is about 0.75°. It is twice the value $\Delta\theta_{max}$, just as it should be. The broadening outside the side maxima should, however, be much smaller according to our simulation model. We must point out that the XRD measures average distortion along a considerable length (1 mm) of the stripe, while the image in the back reflection section topograph shows only a 20 μm thin slice. The back reflection image in Fig. 2(b) shows that individual stripes have some orientational variations along the stripe, which broadens the side maxima in XRD measurements.

Finally, it must be noted that many simplifications have been made in our analysis. We have omitted such physical parameters as the width of the x-ray beam slits and the penetration depth of the radiation. A realistic 20 μm wide slit can be simulated by shifting images. The penetration depth can also be implemented in the simulation. As a result simulations show thicker images in both cases. The substrate under the ELO layer should also become visible in some cases. However, the good image contrast of the seed window cannot be explained simply by absorption or by the slit width. It requires a more sophisticated treatment which takes into account strain-induced enhancement of the diffracted intensity[12] or extinction contrast. Moreover, many effects (e.g., strain in the substrate induced by the mask,[13] deformation of ELO lattice planes due to nonuniform doping,[14] etc.) known to be present in these ELO samples have been neglected. Despite the fact that the situation under study has been simplified our simulation procedure has reproduced the main features of the section topographic images and the XRD curves.

V. CONCLUSIONS

It is concluded that the images calculated using orientational contrast simulations are in a very good agreement with the measured back reflection section topographs of GaAs ELO structures. Only the upper surfaces of the ELO layer and the substrate are used in the simulation. Our interpretation of the topographs and simulations show that the misorientation of the lattice planes increases faster near the center of the ELO layer than at the edges, i.e., the bending radius increases towards the edges of the ELO layer. The model used for simulations predicts the main features observed in the XRD curves of the GaAs ELO layers. Moreover, the calculated shape of ELO lattice planes is in agreement with the measured profile of the upper surface of the layers.

ACKNOWLEDGMENTS

This work is supported in part by Polish Committee for Scientific Research under the Grant No. 8 T11B 030 10, TMR-Contract No. ERBFMGECT950059 of the European Union and the Irish Forbairt International Collaboration Program.

[1] B.-Y. Tsaur, R. McClelland, J. Fan, R. Gale, J. Salerno, B. Vojak, and C. Bozler, Appl. Phys. Lett. **41**, 347 (1982).
[2] L. Jastrzebski, J. Corboy, and R. Soydan, J. Electrochem. Soc. **136**, 3506 (1989), and references therein.
[3] T. Nishinaga, T. Nakano, and S. Zhang, Jpn. J. Appl. Phys., Part 2 **27**, L964 (1988).
[4] S. Zhang and T. Nishinaga, J. Cryst. Growth **99**, 292 (1990).
[5] S. Nakamura *et al.*, Jpn. J. Appl. Phys., Part 2 **36**, L1568 (1997).
[6] T. Tuomi, K. Naukkarinen, and P. Rabe, Phys. Status Solidi A **25**, 93 (1974).
[7] R. Rantamäki, T. Tuomi, Z. R. Zytkiewicz, D. Dobosz, and P. J. McNally, J. Phys. D **32**, A114 (1999).
[8] Z. R. Zytkiewicz, J. Domagala, D. Dobosz, and J. Bak-Misiuk, J. Appl. Phys. **84**, 6937 (1998).
[9] Z. R. Zytkiewicz, Cryst. Res. Technol. **34**, 573 (1999).
[10] R. Köhler, B. Jenichen, H. Raidt, E. Bauser, and N. Nagel, J. Phys. D **28**, A50 (1995).
[11] H. Raidt, R. Köhler, F. Banhart, B. Jenichen, A. Gutjahr, M. Konuma, I. Silier, and E. Bauser, J. Appl. Phys. **80**, 4101 (1996).
[12] I. A. Blech and E. S. Meieran, J. Appl. Phys. **38**, 2913 (1967).
[13] Z. R. Zytkiewicz, J. Domagala, D. Dobosz, and J. Bak-Misiuk, J. Appl. Phys. **86**, 1965 (1999).
[14] Z. R. Zytkiewicz, D. Dobosz, and M. Pawlowska, Semicond. Sci. Technol. **14**, 465 (1999).